Fluorination of (Mg,Cu,Al,Fe)-based LDHs template for conversion materials usable in all-solid state lithium metal batteries

Fabien Eveillard, Katia Guérin, Nicolas Batisse, Kevin Lemoine, Abdelraouf Rouag, Diane Delbègue, Fabrice Leroux

Fluorination of (Mg,Cu,Al,Fe)-based LDHs template for conversion materials usable in all-solid state lithium metal batteries

Fabien Eveillard [a,b], Katia Guérin [b*], Nicolas Batisse [b], Kevin Lemoine [b], Abdelraouf Rouag [b], Diane Delbègue [a], Fabrice Leroux [b*]

[1] *Centre National des Etudes Spatiales, 18 avenue Edouard Belin 31 401 Toulouse Cedex 9, France*
[2] *Université Clermont Auvergne, CNRS, INP Clermont, ICCF, UMR n°6296, 24 Avenue Blaise Pascal, 63178 Aubière, France*

***** Correspondence: KG : Katia.ARAUJO_DA_SILVA@uca.fr Tel.:+33 (0)4 73 40 75 67
FL : fabrice.leroux@uca.fr Tel.: +33 (0)4 73 40 70 36

GRAPHICAL ABSTRACT

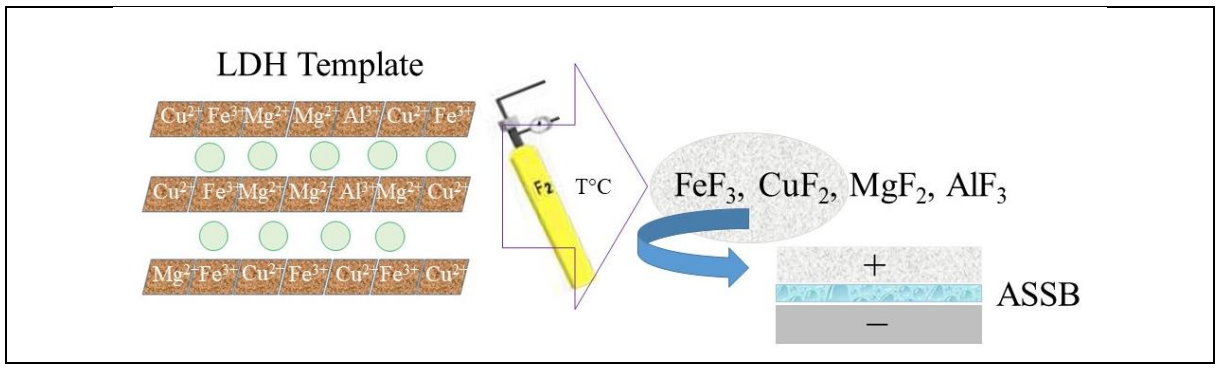

ABSTRACT

Iron and copper fluorides are of interest as conversion cathode materials in lithium batteries but they suffer from high hysteresis and low cyclability, respectively. To overcome these limitations and take advantage of the electrochemical properties of each of the fluorides, fluoride mixtures that combine the two redox centers Fe^{3+} and Cu^{2+} are synthesized using Layered Double Hydroxides (LDH) as a 2D multi-metallic template. Hydrotalcite-type phases

substituted with Cu^{2+} and Fe^{3+} ions are prepared by coprecipitation then fluorinated with fluorine gas in static mode at temperatures chosen according to their thermal evolution monitored by mass spectrometry. After each fluorination treatment, the materials are characterized by X-ray diffraction and most LDH materials are found stable up to 200°C, treatment above leads to the formation of fluorides of each of the cations. The initial dispersion of the cations in the LDH sheets nevertheless allows, after fluorination, a composite of fluorides making them totally accessible to the phenomenon of electrochemical conversion shown here in a metallic lithium battery assembly with a Solid Polymer Electrolyte (SPE). In such All-Solid-State Battery (ASSB) configuration often limiting in terms of columbic efficiency, 76 % the first discharge capacity is recovered in charge for an optimized composition (up to 560 $mAh.g^{-1}$). This good reversibility positions these LDH templates very well for future investigations in the field of electrochemical storage.

Keywords: Layered Double Hydroxide, Solid-Gas Fluorination, Solid-State Lithium Metal Battery

1. INTRODUCTION

Transition Metal Fluorides (TMFs) are emerging as promising cathode materials in Lithium batteries (Turcheniuk et al., 2021). Among the TMFs of particular interest, FeF_3 and CuF_2 are extensively studied in the literature (Hua et al. 2021). Indeed, FeF_3 exhibits a theoretical capacity of 712 $mAh.g^{-1}$ at a voltage of 2.74 V *vs*. Li^+/Li (Eveillard et al., 2020; Guérin et al., 2016; Huang et al., 2019; Shimoda et al., 2020) while CuF_2 displays a theoretical capacity of 528 $mAh.g^{-1}$ at a voltage of 3.55 V *vs*. Li^+/Li (Hua et al., 2014; Krahl et al., 2018; Omenya et al., 2019; Seo et al., 2017). However, TMFs usually suffer from high voltage hysteresis and low cyclability, both related to the dramatic volume change and deep

reduction state involved in the conversion step resulting from the transformation of TMF to LiF and TM (Wu et al., 2020a). Interestingly electrochemical properties for both FeF_3 and CuF_2 are enhanced in ternary metal fluorides of general formula $Cu_yFe_{1-y}F_2$ (Omenya et al., 2019; Seo et al., 2017; Wu et al., 2020a; Wang et al., 2015) obtained by mechanochemistry. This underlines the benefit of mixing fluorides together in particular to optimize the battery energy density (depending on both the capacity and the voltage of the working electrodes). This also prompts us to step further in the level of mixing between fluorides to combine in one material high voltage provided by Cu^{2+} ions and high capacity provided by Fe^{3+} ions. Indeed, the synthesis of such TMFs including both copper and iron cations is really topical to meet the high energy requirements.

In this sense, a Multi-Metallic Template Fluorination MMTF is presented here to prepare similar materials. This synthesis procedure is carried out by solid-gas fluorination using gaseous F_2 reacting with Multi-Metallic Templates MMT of interest. It allows working without water and the formation of a subsequent hydrated phase. This method of synthesis is uncommon, as conventional fluorination methods use a fluorinating solution such as fluorytic sol-gel method with usually trifluoroacetic acid (Erhard and Noack, 2015). In a previous study, fluorination of a 3-dimensional (3D) MMTF, namely Copper-based Prussian Blue Analogue (CuPBA), led either to a fluorinated multi-metallic structure phase at low fluorination temperatures or a CuF_2/FeF_3 two-phase mixture at higher temperatures, all with interesting electrochemical properties compared to a similar composition obtained by mechano-chemistry (Eveillard et al., 2022). After fluorination of the template at 350°C, a first discharge of 878 $mAh.g^{-1}$ and 59% reversibility in subsequent charge was obtained in comparison with 620 $mAh.g^{-1}$ and 68% reversibility for the ball milling reference sample of similar CuF_2/FeF_3 composition. Another article reports the formation of multi-metallic pyrochlore fluorides by gaseous fluorination of multi-metallic ammonium fluoride precursors

(Lemoine et al., 2021). The oxidation is found to proceed through a topotactic mechanism; however, the obtained materials show poor electrochemical properties. Among the MMTs of interest, Metal Organic Frameworks (MOFs) exhibit a tunable multi-cation forming large open structure that should facilitate fluorine diffusion (Glowniak et al., 2021; Liu et al., 2020; Sun et al., 2019; Xia et al., 2016). The preliminary synthesis of fluorinated organic linkers enables the formation of various fluorinated MOF structures (Chen et al., 2013; Pachfule et al., 2011; Pachfule et al., 2016) whereas the calcination of a non-fluorinated MOF template exposed to a fluorinating agent promotes the formation of analogous metal fluorides with interesting electrochemical features (Liu et al., 2020; Wu et al., 2021; Zhang et al., 2019). However, the large quantity of organic linkers in MOFs hinders their use as solid-gas fluorination precursors, since it may lead to the formation of insulating carbon fluoride CFx and/or highly toxic gaseous by-products.

To overcome this issue while retaining the benefit of an accessible open structure as well as to generalize the MMTF concept, Layered Double Hydroxides are considered here as templates. Indeed, these versatile compounds are known to present a lamellar structure and a chemical composition tunable by a simple synthesis using pH-regulated metal ion coprecipitation, making them interesting for innovative applications and industrial transfer (Taviot-Guého et al., 2018). These compounds have the general formula $[M_{1-x}^{2+}M_x^{3+}(OH)_2].A_{x/n}^{n-}.mH_2O$ with M^{2+} and M^{3+} divalent and trivalent cations, respectively, and interlayer anions A that compensate the excess of charge of the positive layers. In order to compare the templates between each other as much as possible and in particular between the 3D PBA (Eveillard et al., 2022) and the 2D LDH, the cation composition is selected to form similar ratios between CuF_2 and FeF_3 fluorides.

Such cationic LDH compositions have already been explored in literature, either with only the couple Cu^{2+}/Fe^{3+} in the cationic sheets (Nejati et al., 2013; Wang et al., 2021; Zubair et al.,

2021) or mixed with other cations like Zn^{2+} (Lu et al., 2016), Co^{2+} (Lu et al., 2019), Ni^{2+} (Wang et al. 2018), Mg^{2+} (Zhang et al., 2022) or Mg^{2+}/Al^{3+} (Carja et al., 2001; de Melo et al., 2021; Guo et al., 2012). Among these types of Cu/Fe compositions identified, particular attention is given here to Mg/Al/Cu/Fe cationic compositions. The MMTF applied to the LDH compositions is expected to form a composite of fluorides including domains of MgF_2, AlF_3, CuF_2 and FeF_3. Additionally, TMFs are known to be reactive towards organic electrolytes, especially CuF_2 used in this study (Celik-Kucuk et Abe, 2021). Solid electrolytes are preferred since the end goal is to obtain an All-Solid-State Battery (ASSB) that is safer when embedded in autonomous energy stockage systems such as those needed in space applications. In that sense, the solid polymer electrolyte (SPE) PEO/LiTFSI (Poly Ethylene Oxide impregnated with Lithium bis(trifluoromethanesulfonyl)imide) is used, since it is known to be efficient with FeF_2 as reported by Huang et al. (Huang et al., 2019). However, a special attention should be paid since recent article reports that PEO might not be suitable for electrode materials containing copper fluoride (Omenya et al., 2019).

Beforehand, the thermal transformations of synthesized LDH materials are monitored using thermogravimetric measurements coupled with evolved gas analysis by mass spectrometry (MS TGA). Fluorination temperatures of interest are selected as a function of the major thermal events. Structural changes occurring after fluorination are characterized by X-ray diffraction (XRD). The local structural change reported in supporting information is followed as a function of fluorination temperature, reporting the near-edge structure at the two transition metal absorption K edges.

An All-Solid-State Battery (ASSB) set-up using PEO/LiTFSI as the Solid Polymer Electrolyte (SPE) is used to explore the electrochemical mechanism of the fluorinated composite materials. Cyclic voltammetry with a scan rate of 20 $\mu V.s^{-1}$ is used to scrutinize the insertion and conversion mechanisms over a wide-open potential window (50 mV to 4.1 V *vs*.

Li^+/Li). The shape of the CVs is compared between fluorinated LDH after fluorination at 200 and 350°C. Finally, the voltage as a function of the capacity of each candidate is recorded in galvanostatic mode.

2. MATERIALS AND METHODS

3.1. Material synthesis and fluorination

For the synthesis of LDH of general theoretical composition $(Mg, Cu)^{2+}(Fe, Al)^{3+}Cl(OH)_6 \cdot nH_2O$, hydrated metal chlorides and sodium hydroxide were used as supplied by Aldrich, without further purification. The hydrotalcite-like materials were prepared via coprecipitation method. Experimentally, 100 mL of a solution of each $CuCl_2$, $MgCl_2$, $AlCl_3$ and $FeCl_3$ hydrated salt (0.01 $mol.L^{-1}$) was prepared. Three different solutions of cationic mix $Cu^{2+}/Mg^{2+}/Al^{3+}/Fe^{3+}$ (1.5/1.5/0.5/1) (1.5/1/0.25/1) (1.5/0.5/0/1) were considered for the preparation of three different theoretical (M^{2+}/M^{3+} = 2:1) LDH cationic sheet compositions $(Cu_{1.5}Mg_{1.5})^{2+}(Al_{0.5}Fe_1)^{3+}$; $(Cu_{1.5}Mg_1)^{2+}(Al_{0.25}Fe_1)^{3+}$; $(Cu_{1.5}\ Mg_{0.5})^{2+}(Fe_1)^{3+}$. Solutions of the reactants were added to the reactor with peristaltic pumps at a constant flow of 2.0 $mL.min^{-1}$ for 3 h under a nitrogen atmosphere, to avoid the carbonate contamination from air. The pH was kept constant at different values (7.5, 8.5, 9.5 and 10.5 ± 0.1) through the addition of a sodium hydroxide solution (0.1 $mol.L^{-1}$) by an automated regulation system. After a 3 h aging, the slurries were centrifuged and finally washed several times with distilled water. After drying, the products were recovered as fine powders and characterized. Only the $(Cu_{1.5}Mg_{0.5})^{2+}(Fe_1)^{3+}$ chlorinated LDH product synthesized at pH = 10.5 (theoretical composition $[(Cu_{0.5}Mg_{0.17})^{2+}(Fe_{0.33})^{3+}(OH)_2]\ Cl_{0.33}\ .\ xH_2O$) was then used as a fluorination precursor.

A dedicated equipment consisting of a passivated cylindrical nickel reactor of approximately 50 cm in length and 1 L in volume was used for solid gas fluorination using special care. Pure

molecular gaseous fluorine from Solvay Fluor (purity 98-99 % v/v with HF max. 0.5 % v/v and other gases, mainly O_2/N_2 at about 0.5 % v/v) was used for all experiments. A 20 cm long sample holder coated by passivated nickel was loaded with two hundred milligrams of a finely grounded powder recovered after LDH synthesis. The reactor was first degassed at RT by flushing gaseous nitrogen for 1h to remove any moisture and oxygen presences and placed under primary vacuum. To ensure heating, the reactor tube was lined by a horizontal tube furnace, ensuring a homogeneous temperature zone of approximately 10 cm at the centre of the reactor. The furnace was then heated at a 5°C.min^{-1} rate until the desired fluorination temperature was reached (in between RT and 350 °C). Fluorine was injected at 40 mL.min^{-1} up to 1 bar and maintained during 3 hours in the closed reactor in a static mode. After reaction and when the temperature was below 100 °C in the reactor, nitrogen was injected to remove all the fluorine gas. The powders were then stored under argon in a glove box to avoid degradation by air.

3.2. Structural characterization

A Panalytical X-Pert Pro diffractometer equipped with a Cu Kα1 source diffracted beam monochromator and a linear X'celerator detector and using a home-made sample holder closed to under static inert argon was used to collect X-ray diffraction (XRD) data. Recording conditions were with a counting time of 108 seconds associated with an angle step size 2θ of 0.0167° in 10-80° range. Profex software was used for patterns matching (Doebelin et al., 2015).

Using SOLEIL Synchrotron facilities (France), X-ray absorption spectroscopy (XAS) measurements at both K-edges of copper and iron were performed at 80 K in transmission mode. The ROCK beamline was equipped with a sagittal focusing Si (220) monochromator (Briois et al., 2016). The intensity of the monochromatic X-ray beam was measured by the detectors placed in the ionization chambers. Dispersed with cellulose, the powders were

pressed into pellets. Any contact of the fluorinated products with air was avoided by placing the pellet in Kapton. Three successive scans with energy steps of 0.5 eV were performed to ensure reproducibility of the measurements. For each scan, calibration in energy was possible by simultaneously recording absorption measurements of Fe and Cu metal foils. The data were averaged and normalized using ATHENA software (Ravel et al., 2005), and the resulting pseudo radial distributions (PRD) were not corrected for phase shift.

A Netzsch STA F3 Jupiter apparatus was used for thermal analyses. Before any measurements, three successive vacuum cycles were applied to clean the sample chamber. Each sample was heated using a temperature slope of 10°C.min^{-1} and a constant flux of 70 ml.min^{-1} either under He or dry air (80/20 % v/v N_2/O_2). An average of 20 mg of powder was placed in an alumina crucible with a lid in the glove box to avoid contact with air during the transfer to the TG sample chamber. The analysis was processed by mass spectrometry (Netzsch Aeolos Quadro) and the main signals of the evolved gases were shown stacked for qualitative comparison.

The different samples were characterized by Scanning Electron Microscopy (ZEISS Supra SEM operating at 3 kV).

3.3. Electrochemical characterization

A cycling temperature of 60°C was used to favour lithium diffusion in the solid electrolyte used. Beforehand, each powder (MF) was mixed for 6 h at 350 rpm in a planetary ball milling with acetylene black (AB) to improve its electron conductivity using a weight ratio MF/AB of 50/50. All subsequent steps were performed in an argon-filled glove box. The milled powder MF and AB was mixed with PVDF powder as a binding agent in a weight ratio of 90:10, and the resulting mixture was then dispersed in propylene carbonate to obtain a homogeneous slurry. Wet deposits were syringed onto stainless-steel grids (14 mm diam., 0.2 mm thickness) and subsequently dried at 80°C under vacuum (usually 1.8-2.7 mg of active mass of MF). The

resulting cathodes were assembled in a two-electrode coin cell (CR2032) with lithium metal disk (1 mm thick - Aldrich) acting as both negative and reference electrodes, *i.e.* voltage values expressed *vs* Li^+/Li. A 200 µm-thick PEO-LiTFSI membrane (H-Polymer, NEI Corporation) was placed between the cathode and lithium. Solubilized PEO-LiTFSI powder in 14 wt. % of pure acetonitrile was poured on a PTFE foam leading to an amorphous polymer presenting a glass transition temperature below 0°C associated to an ionic conductivity of about 5.10^{-5} $S.cm^{-1}$ at RT.

Electrochemical measurements were carried out on a VMP3 or a BCS Biologic instrument. Relaxation time of no less than 5 h was performed to stabilize the open circuit voltage (OCV). Cyclic voltammetry was performed at 0.02 $mV.s^{-1}$ in the potential range 50 mV to 4.1 V. Galvanostatic experiments were carried out in the potential range 1-4.1 V with a C/50 and C/250 per $mA.g^{-1}$ of active mass current density for discharge/charge, respectively.

3. RESULTS AND DISCUSSION

3.1. Optimization of the synthesis

A range of materials considering multiple substitution in the variable composition (Cu, $Mg)_2$(Fe, Al) was studied: XRD results of three types of LDH with different cationic sheet compositions are presented in Fig. S1. As the overarching target is here on the composition adopting the less non-electrochemical cation and keeping the ratio of Cu/Fe of 3/2 similar to PBA, the LDH of theoretical composition $(Cu_{0.5}Mg_{0.17})^{2+}(Fe_{0.33})^{3+}(OH)_2\,(Cl)_{0.33}\,.\,xH_2O$ is retained in the following. A chloride LDH form is here preferred since the reaction of chlorine with fluorine is expected to be total without any by-product.

Figure 1 shows the effect of the pH value applied constant during the coprecipitation. At pH of 7.5 and 8.5, a paratacamite phase is formed. Indeed, all the diffraction peaks are assigned to this phase (ICSD 64956). Paratacamite is a mineral of composition $Cu_2(OH)_3Cl$ that is found

to crystallize in space group *R*3 (Fleet, 1975). Jahn-Teller cation Cu^{2+} is well-known to destabilize the edge-sharing LDH sheets when in too much quantity converting LDH either to botallackite-type structure (Jiménez-López et al., 1993; Leroux et al., 2002) or to two-dimensional $Cu_2(OH)_3X$ paratacamite as observed here for X = Cl (Fujita et al., 1997). Increasing pH to 9.5 results in the formation of CuO (monoclinic with *C*2/*c* space group) while at 10.5, a LDH phase is dominant with a very small amount of CuO. The presence of the observed phase domains agrees with recent literature covering the structural changes as a function of pH values between 7 and 13 (Jang et al., 2021): below pH = 8, malachite of composition $Cu_2CO_3(OH)_2$ is formed, while in our case it is paratacamite due to the presence of chlorine anion. At pH of 8 to 9, a mixture of malachite and LDH is then observed, a pure LDH phase is observed at pH = 10, it is pH =10.5 in our case with the presence of small quantity of CuO. Increasing the pH up to 12 leads to the presence of CuO only (Jang et al., 2021).

For the LDH phase, the first three diffraction peaks are attributed to the harmonic contribution (00ℓ) of the layered structure, and the corresponding basal spacing of 7.8 nm agrees well with the formation of a chloride LDH phase (Constantino et Pinnavaia, 1995). The broad contribution observed at around $2\theta = 60°$ comes from the overlap between two diffraction peaks (110) and (113). Usually the position of (110) informs on the intra-layer order and its value is related to the combination of cation edge-sharing octahedral sites. However, it is difficult here to apply this relation because of the excessive width of peak. The exact quantification of the CuO small impurity is also difficult to establish from any XRD pattern refinement for the aforementioned reason.

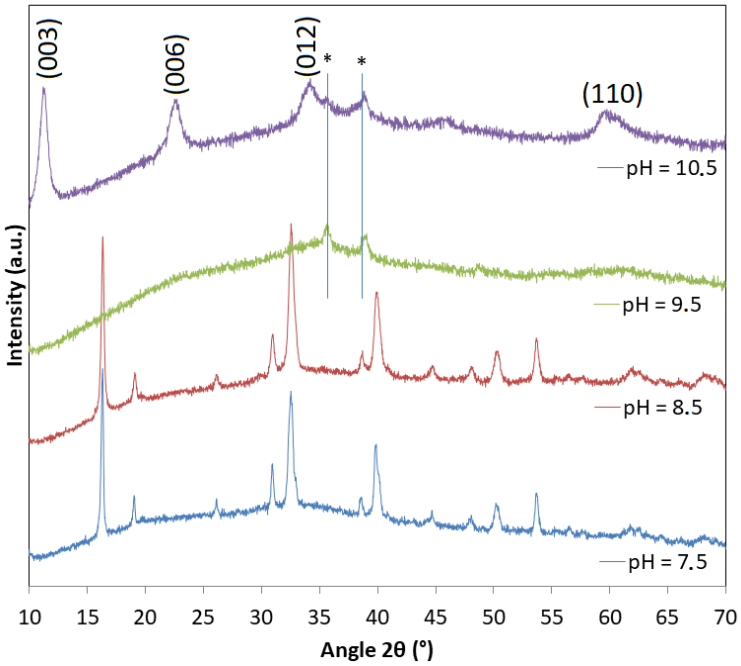

Fig. 1. XRD patterns of the targeted LDH composition $(Cu_{0.5}Mg_{0.17})^{2+}(Fe_{0.33})^{3+}(OH)_2\ (Cl)_{0.33}.\ xH_2O$. The value of pH for the coprecipitation is indicated. One note that the experimental composition deviates from the initial cation input. * are the two most intense diffraction peaks for CuO at 2θ = 35.6° (111) and 38.8° (022).

3.2.Chemical analyses

The sample prepared at pH of 10.5 is analysed by ICP AES as well as by TG coupled MS. From the chemical analyses, the input ratio of Fe/Cu/Mg of 33/50/17 is found to deviate to 31.4/30.3/38.3 (Supporting), thus indicating that a part of the cations Cu^{2+} has not precipitated to form the LDH phase of pyroaurite type. This can be explained by the fact that high pH value is usually not adapted to stabilize Cu^{2+} in LDH, but is more prone to form cupric hydroxide or cupric oxide. For the lower content of Fe^{3+} cations compared to its initial input, it is unexpected. The initial ratio is Fe/Mg of 2 and Cu/Mg of 3 with M^{2+}/M^{3+} of 2, while it is found for both Fe/Mg and Cu/Mg of less than 1 but keeping the ratio M^{2+}/M^{3+} of 2.

Such chemical deviation from the initial input is usually observed (when chemical analyses were performed) on various Cu-containing LDH phases such as Cu, Zn, Al hydrotalcite-like materials (Behrens et al., 2010). It is usually explained by the fact that the edge-sharing layout between $Cu(OH)_6$ with other $M(OH)_6$ octahedra inside the sheets is strongly restrained by elongation and compression due to Jahn-Teller distortion of the cations Cu^{2+}, thus forming other phases or else remaining in solution when the Cu phases, *i.e.* paratacamite at pH < 9 or CuO at pH > 11, are not stable. In other chemical compositions, it leads to a change of structure as for $(Mg_{4-x}Cu_x)Al_2OH_{12}CO_3$, nH_2O where the space group is modified from rhombohedral to monoclinic when increasing the copper content (Intissar et al., 2015), or a change in the local structure as for Cu, Zn, Al where the incorporation of Cu^{2+} induces the presence of AlO_4 species (Wu et al., 2020b) to compensate the constraints imposed by the Jahn–Teller effect of copper. Concerning the lower content in Fe^{3+} cations, it may be due to the presence of Cu^{2+} cations since the pyroaurite type phase is known to be formed at this pH value or a little higher (Hansen and Koch, 1995; Rozov et al., 2010). This deviation in the chemical composition will need further investigation by varying copper substitution to establish a suitable solid solution (Cu,Mg)Fe LDH-type phases.

TG-coupled MS analysis is carried out for the sample (see Fig. 2). To complete this analysis, XRD was performed on residues obtained after heating under vacuum at 150°C, 200°C and 350°C (denominated afterwards as LDH V150, LDH V200 and LDH V350 respectively): the resulting diffractograms are presented in Fig. S2. In between RT and 215°C, the transformation step is attributed to the dehydration of the product but also to a partial dehydroxylation as observed by the intensity of H_2O and OH signals. The loss of mass is therefore both associated to the degree of hydration of the product but also to an amorphization of the LDH structure as shown in the associated X-ray diffractogram after heating to 150°C in vacuum (see Fig. S2). This amorphization is related to a destabilization of

290 the interlamellar space and a reduction of the average crystallite size. Nevertheless, the
291 presence of peaks corresponding to the (003), (006), (012) and (110) difraction peaks of the
292 pristine LDH structure indicates that the template LDH structure is at least partially
293 maintained after this heat treatment. With increasing fluorination temperature, the interlayer
294 distance increases as shown by the (003) shift for LDH V200, and counter-intuitively, it
295 corresponds to an increase in the interlayer distance due most probably to reorganization
296 during the dehydration process.

297 Fig. 2 shows that in between 215 and 500 °C, the presence of CO_2 and H_2O release is related
298 to the transformation of LDH into Lamellar Double Oxides (LDO) upon calcination as shown
299 in the literature (Huang et al., 2015). The origin of the CO_2 is a contamination of the LDH
300 powder, often occurring during the successive slurry separations from the supernatant and
301 washing/drying steps, in particular for LDH prepared at high pH value. The relative amount
302 of carbonate anions is calculated from the MS relative intensity and the chemical composition
303 is deduced as $Cu_{0.31}Mg_{0.38}Fe_{0.31}(OH)_2(CO_3)_{0.05}Cl_{0.21}.0.45\ H_2O$. The structural transformation
304 associated within this temperature region is characterized by a strong amorphization of the
305 structure as evidenced from the X-ray diffractograms of the residues obtained after heating
306 under vacuum at 200 (LDH V200) and 350°C (LDH V350) and the absence of peaks
307 associated with the (006) planes of the LDH structure (see Fig. S2). It is interesting to note the
308 presence of a diffraction peak associated with the (003) diffraction peak of the LDH structure
309 around $2\theta = 11°$ in LDH V200 and absent in LDH V350: a partially crystallized LDH phase is
310 thus preserved at 200 °C while it is absent after 350°C. Also, the CuO peaks at 350°C being
311 less intense than the resulting amorphous phase after 350°C confirms the very low amount of
312 this by-product with the LDH phase.

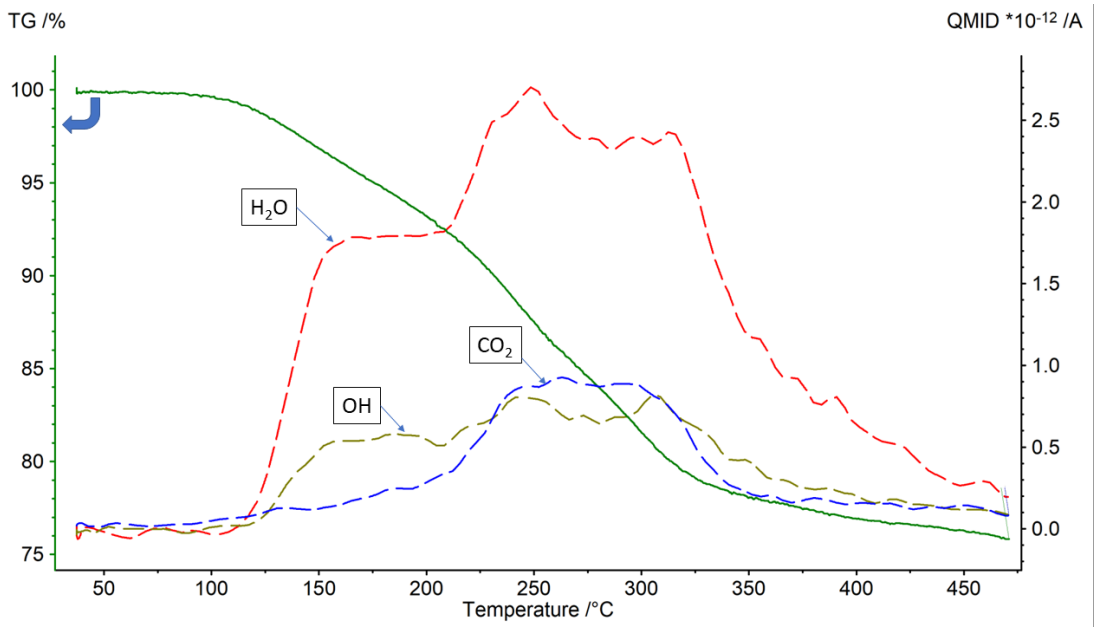

313

314 **Fig. 2.** TG-MS analysis of the sample $Cu_{0.31}Mg_{0.38}Fe_{0.31}(OH)_2(CO_3)_{0.05}Cl_{0.21}$. $0.45H_2O$

315 under Helium (Heating ramp: 10 °C.min^{-1})

316

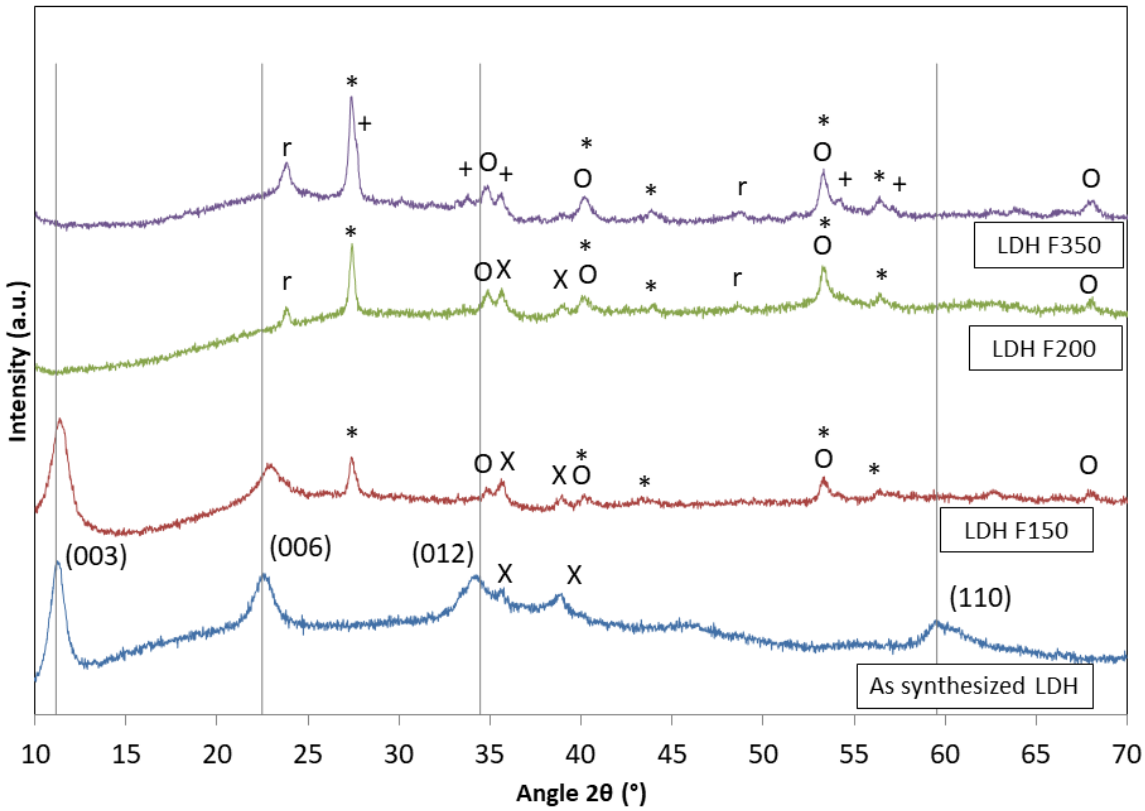

317

Fig. 3. XRD patterns of $Cu_{0.31}Mg_{0.38}Fe_{0.31}(OH)_2(CO_3)_{0.05}Cl_{0.21}$. $0.45H_2O$ as a function of the fluorination temperature and identification of the crystallized phases: x CuO (ICSD#16025); O FeOF (ICSD#2875) ; + CuF_2 (ICSD#71833) ; * MgF_2 (ICSD#394) ; r r-FeF_3 (ICSD#41120)

The structures of LDH fluorination products obtained at different temperatures are first studied by XRD: the as-synthesized LDH was fluorinated at 150°C, 200°C and 350°C (denominated afterwards as LDH F150, LDH F200 and LDH F350 respectively). The thermal treatment under molecular F_2 is known to be efficient in obtaining fluorides at low temperature as 100°C (Louvain et al., 2014). However, in the present results, the layered structure of the pristine LDH remains after fluorination at 150°C. Using static conditions favours substitution of OH^- groups by F^- (Myung et al., 2013). However, the intra-organization is not present anymore (Fig. 3). Indeed, the absence of the diffraction peak (110) at 2θ close to 60° suggests that the intra-sheet organization is strongly disrupted. This is explained by the presence of crystallized phase MgF_2 and FeOF showing that an important quantity of cations constituting LDH sheets is reacting. Most probably their ingress out of the LDH structure creates lacunas and voids, thus cancelling the coherence length in the in-plane. While the fluoride MgF_2 is formed first, it is then followed by r-FeF_3 at 200 °C, LDH structure has totally disappeared while low-crystallized CuO still remains present. Presumably the fluorination temperature of 150°C is not sufficient to convert it to copper fluoride. Indeed, the transformation of CuO into CuF_2 is known to begin at 300°C and is only complete above 500°C under pure molecular gaseous fluorine (Haendler et al., 1954). A relatively well-crystallised MgF_2 phase is noted: this compound is the only binary fluoride identified in the product, which suggests that the crystallisation temperature of MgF_2 is lower than that of FeF_3 or CuF_2. Indeed, magnesium fluoride is easily formed at 25°C from HF fluorination of

oxygen-based magnesium source (Skapin et al., 2009) whereas rhombohedral iron trifluoride is only obtained above 200°C under pure molecular fluorine (Guérin et al., 2016).

FeOF was successfully prepared in literature both by solvothermal reaction (Fan et al., 2015) and wet-chemical method (Zhu et al., 2015) using a FeF_3 precursor. In both cases, the synthesis was performed around 200°C which is consistent with our XRD observations. In the case of LDH fluorination, crystallisation of FeOF could be favoured over FeF_3 at low fluorination temperatures especially at 150°C. Finally, CuO is converted to CuF_2 after treatment at 350°C, as observed with the shoulder at 2θ around 27° and 55°.

The occurrence of the different crystallized phases as a function of the temperature of fluorination agrees with the comparison of the standard enthalpy of formation of the related crystalline phases as follows (at 298,15 K): $\Delta H_f°$ (MgF_2) = -1124 kJ/mol^{-1} (Rudzitis et al., 1964) < $\Delta H_f°$ (FeF_3) = -989 kJ/mol^{-1} (Johnson, 1981) < $\Delta H_f°$ (CuF_2) = -540 kJ/mol^{-1} (Walsh et al., 2012). It helps to understand that – 1) MgF_2 rutile type crystal crystallizes first with the intense diffraction peaks at 2θ ≈ 26° and 40° for (110) and (111), respectively, - 2) r-FeF_3 crystallizes next to MgF_2, and – 3) CuF_2 crystallizes last at 350°C.

To further corroborate the existence of the fluorinated LDH phases, XAS analyses of the fluorinated product, the LDH precursor and reference fluorides recorded at both iron and copper K edges are shown in Fig. S3.

From these measurements, the iron and copper environment in the LDH precursor and in LDH F150 are quite similar. Furthermore, the iron environment differs from that of FeF_3, confirming a local iron environment in LDH F150 different from that of a binary fluoride and closer to that present in the non-fluorinated precursor. These observations confirm that fluorination at 150°C is not sufficient to break the LDH structure. The LDH fluorination

366 product obtained at 150°C therefore shows a crystallised LDH phase coexisting with MgF_2
367 phase.

368 To complete these characterizations, the comparison of the thermograms obtained after
369 fluorination at 200°C and 350°C (see Fig. S4) shows a mass loss at 150°C corresponding to
370 the dehydration of the different products (hydration due to their exposure to air before
371 measurements). Apart from this thermal event, all the fluorination products are thermally
372 stable at least up to their fluorination temperature, which confirms the anchoring of fluorine in
373 these fluorination products. According to these analyses, the product obtained after
374 fluorination at 350°C is relatively stable up to 1000°C, its thermogram showing no significant
375 mass loss up to this temperature. On the other hand, the thermogram LDH F200 shows mass
376 losses resembling the non-fluorinated LDH precursor, particularly at 600°C. This may suggest
377 the presence of a LDH phase not only in the fluorinated product at 150°C as confirmed by
378 XRD but also in the fluorinated product at 200°C. Thus, these results indicate that the
379 conversion of the LDH phase to fluoride analogues is not complete at 200 °C which is
380 consistent with the XRD results obtained on the residues after heating in vacuum of the LDH
381 template. However, it is difficult to quantify this phase in the final product.

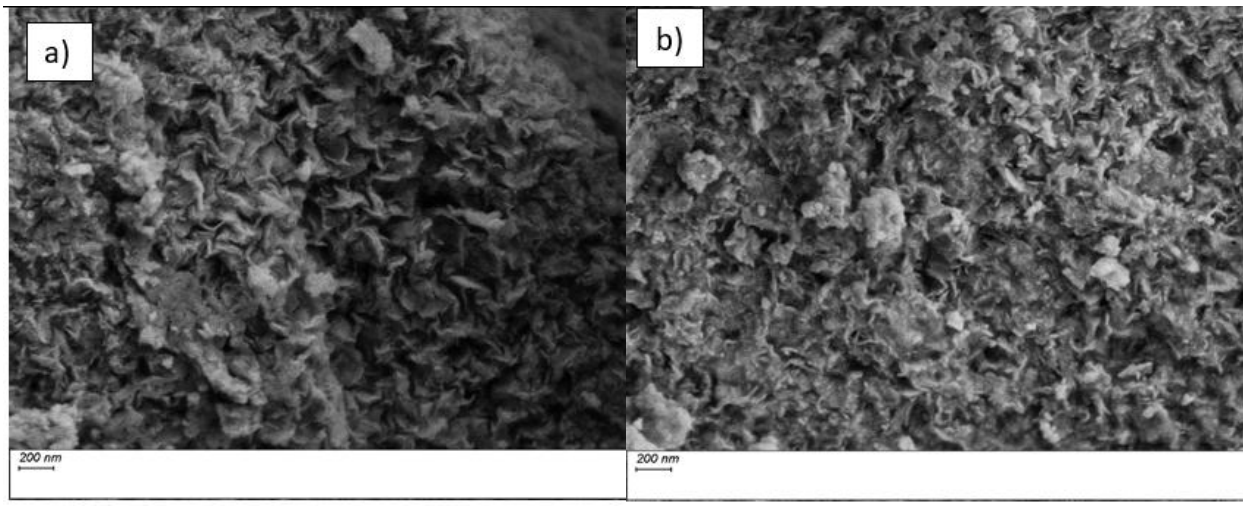

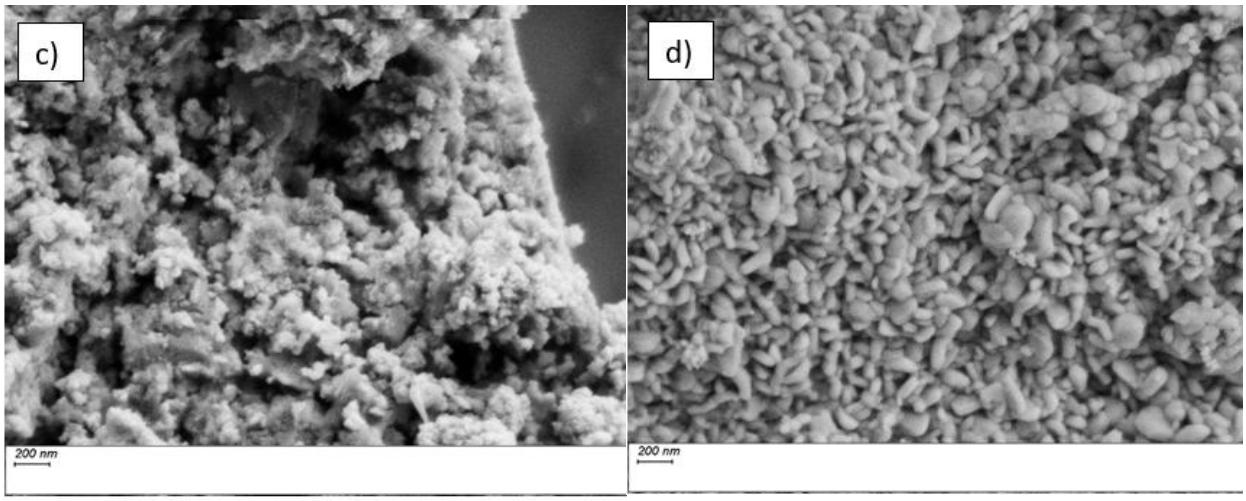

Fig. 4. SEM picture of LDH (a) before and after treatment at (b) 150°C, (c) 200°C and (d) 350°C under F_2.

SEM pictures are compared before and after fluorination. The shape of LDH particles before treatment is consistent with a lamellar material and flakes are observed. Such observation is still available for the treatment at 150°C under F_2, thus indicating as stated by XRD that the LDH layered structure is mostly maintained. After treatment at 200°C, the flakes are no longer visible but small geometric shapes are present. At this step, the fluorination appears as having ground the pristine structure. A much more homogeneous morphological distribution appears after 350°C and the particles are oblong worm-shaped not classical of porous 3D-rhombohedral FeF_3 (Guérin et al., 2016) or 3D micrometric dense CuF_2 (Hua et al., 2014).

2.3. Electrochemical study

Firstly, the cyclic voltammetry cycle at 0.02 $mV.s^{-1}$ obtained on each of the three products is presented in Fig. S5. The redox activity of the LDH fluorination products increased with increasing fluorination temperature. This difference in activity cannot be attributed to a change in oxidation state, as XAS and XRD analysis confirmed that the oxidation states are

399 kept for Cu^{2+} and Fe^{3+} based on the XAS white line position study for these two transition
400 metals and for Mg^{2+} due to the formation of MgF_2 found by XRD. It can be related to a
401 difference in the electrochemical activity of the stabilized phases in each of the three products.
402 Indeed, according to the characterization of the fluorinated materials, the conversion of the
403 LDH matrix to the analogous fluorides occurs gradually without an intermediate structure. By
404 assuming that the LDH phase formed is less electrochemically active than the fluoride
405 analogues, an improvement in redox activity would be observed as a function of the rate of
406 transformation of the LDH template into fluoride analogues. This hypothesis is based on the
407 difference between the two structures regarding the accessibility to cations and also
408 concomitantly the electronic conduction paths for the reduction of these cations. Indeed,
409 phase total conversion implies the reduction of redox active cations to metal state and the
410 formation of LiF. Following this reasoning, this explains a slightly lower redox activity for
411 LDH F150 due to the proportion of LDH template identified by XRD. Even if the differences
412 in current densities measured between LDH F150 and the other two samples are small
413 because of the slow cycling rate, the redox peaks are more defined with a higher temperature
414 of fluorination of 350°C (Fig. 5). Indeed, a more defined redox peaks after fluorination at
415 350°C compared to that obtained at 200°C is the consequence of the progressive
416 crystallization of the single fluorinated metal phases between these two temperatures but also
417 of the absence of LDH phase in the fluorination product at 350°C as shown by the TGA MS
418 analyses. A better crystallization and the absence of LDH template in LDH F350 lead to a
419 clear separation between the redox domains resulting in an electrochemical mechanism
420 proceeding in distinct electrochemical steps.

421 Finally, it is interesting to note that the general trend observed in the evolution of the
422 electrochemical mechanism of LDH fluorination products as a function of the fluorination
423 temperature is different from that observed for fluorinated CuPBA template (Eveillard et al.,

2022). Indeed, in the case of the fluorination of CuPBA, an intermediate structure ($[Cu(H_2O)_4]_3.(FeF_6)_2$ is observed at 200 °C and CuF_2 and FeF_3 crystallize at higher temperatures, while for LDH, the fluorination products (MgF_2, CuF_2 and r-FeF_3) are observed from 200°C. These observations confirm the existence of fluorination mechanisms different between the two inorganic templates. For CuPBA after fluorination at 200°C, it was found to strongly alter the electrochemical performances. This reduction in redox activity was explained by the high density of redox centers at 200°C, due to a significant rearrangement of the local environment of Cu^{2+} ions at this temperature. The evolution of the redox activity as a function of the fluorination temperature observed for CuPBA was then: CuPBA F200 < CuPBA F140 < CuPBA F350.

In the case of LDH, such topochemical reaction of fluorine replacing hydroxide anions into the cationic sheets leads to a progressive structural conversion of the template to fluoride analogues, the rate of fluorination being as a function of temperature. The LDH thermally treated by molecular F_2 phase is less electrochemically active than the simple fluoride phases according to the first voltammetry cycle, the evolution of the redox activity is simply related to the rate of conversion of the LDH template, hence the observed evolution: LDH F150 < LDH F200 < LDH F350.

In the following it should be noted that intensity is reported per mass of electroactive material.

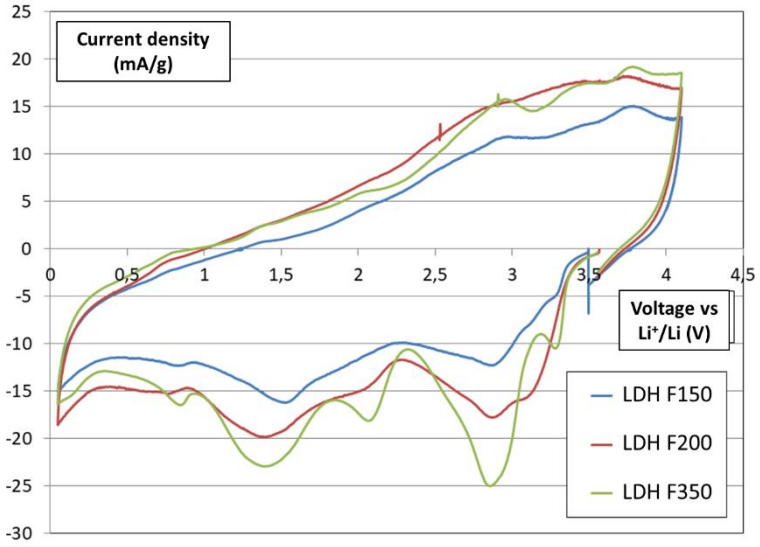

Fig. 5. Comparison of the first cycle of cyclic voltammetry at 0.02 $mV.s^{-1}$ on the LDH fluorination products at 150, 200 and 350 °C, The current density was determined by dividing the measured current by the mass of LDH thermally treated by molecular F2 product contained in the deposit.

The behaviours of LDH F150, LDH F200 and LDH F350 are then studied in more detail in Fig. 5. For this comparison, it is important to consider the electrochemically active phases both in the 1 - 4.1 V *vs* Li^+/Li potential window and in the extended 0.05 - 4.1 V window. For the calculation of current density and capacitance for LDH thermally treated by molecular F_2, assuming a cathode composition (0.31 CuF_2 + 0.38 MgF_2 + 0.31 FeF_3) resulting from the total transformation into analogous fluorides of the metal composition of LDH characterized by ICP AES (see Table S1). Only the electrochemically active part (0.31 CuF_2 + 0.31 FeF_3) of the LDH thermally treated by molecular F_2 deposit is considered while 26.3 % of the mass of the LDH deposit is composed of MgF_2 and is therefore electrochemically inactive both in cyclic voltammetry and in galvanostatic cycling. The presence of this phase will not be

458 considered in these calculations of current density and capacity. Indeed, MgF_2 phase may be
459 minimized later by different processes, whether in the non-fluorinated LDH precursor by
460 working on the stabilization of the copper within the sheets or in the fluorinated precursor
461 using "selective etching" for example. LDH F150 appears as less efficient than the two others
462 which as a consequence were the only ones to be subsequently measured in galvanostatic
463 mode.

464 The comparison of galvanostatic cycling between LDH F200 and LDH F350 is displayed in
465 Fig.6. These measurements confirm a better definition of the redox steps in LDH F350 than in
466 LDH F200 as already observed on the CV curves. A comparison between the expected
467 theoretical capacity and the experimental capacity of the first discharge is also given in Table
468 I.

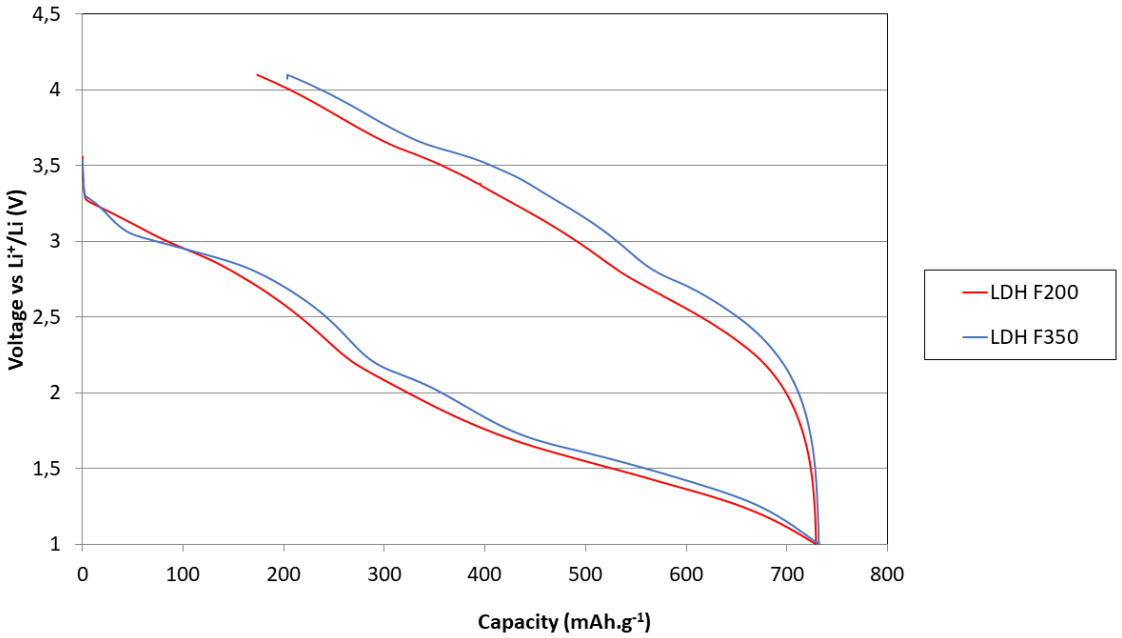

469

470 **Fig. 6.** Galvanostatic cycling of LDH F200 and LDH F350 with current densities of 13.6
471 $mA.g^{-1}$ per active mass (CuF_2 + FeF_3), 2.7 $mA.g^{-1}$ in charge.

472

Table 1: Experimental and theoretical capacity values for the two LDH thermally treated by molecular F_2 compared to pure FeF_3 and CuF_2 electrochemical behaviors and the predicted mixture performance.

Sample	LDH F200*	LDH F350*	FeF_3**	CuF_2**
Q_{exp}(1D) ($mAh.g^{-1}$)	731	731	740	560
Q_{exp}(1C) (%)	76	73	67	23
Q_{theo}(1D) ($mAh.g^{-1}$)	626	626	712	528

Q_{exp}(1D): experimental capacity of the 1st discharge considering the electrochemically active part of the LDH thermally treated by molecular F_2 ($mAh.g^{-1}$); Q_{exp}(1C): capacity recovery in 1st charge (%); Q_{theo}(1D): theoretical capacity considering the electrochemically active part of the LDH thermally treated by molecular F_2; *composition: (0.31 CuF_2 + 0.31 FeF_3 + 0.38 MgF_2), ** see Table S1.

The capacity obtained in the first discharge of LDH F200 and LDH F350 is slightly higher than the theoretical capacity expected for their total conversion as shown in Table 1 and higher than the value registered for a mixture FeF_3/CuF_2 mechanically ground (Fig. S6). This suggests a full reduction of the electrode material has taken place, while the excess capacity being probably due to irreversible reactions as it is already the case for pure FeF_3 and CuF_2 (galvanostatic cycling presented in Fig. S5). The average reaction potential of the two LDH thermally treated by molecular F_2 is slightly lower than pure CuF_2 and FeF_3. Such observation may be related to the presence of the insulating and electrochemically inactive MgF_2 phase, causing an increase in polarization and a lowering of the reaction potentials in discharge. One should not discard possible irreversibility caused between CuF_2 domains and PEO as well as the phenomenon of Cu electroplating on Li anode (Omenya et al., 2019). However, the

retention of capacity in the first charge is interesting for the two LDH thermally treated by molecular F_2. Up to 10 cycles have been performed whereas the retention of capacity for either FeF_3 or CuF_2 in ASSB fails strongly after few cycles (see Fig. S7 for one and half cycle and Fig. S8 after 10 discharges). The better performance is reached for LDH F350 with a retained capacity of 175 $mAh.g^{-1}$ at the tenth cycle whereas for LDH F200, it is of about 150 $mAh.g^{-1}$. For this preliminary study such value is interesting and efforts concerning the electrode formulation and its interaction with the polymer electrolyte are further needed.

4. CONCLUSION

Taking advantage of the composition versatility regarding cation substitution in LDH, copper-iron based LDH compositions are selected to minimize the proportion of structuring ions but electrochemically inactive Mg^{2+} and Al^{3+} added to the substituted LDH phases. A LDH phase of theoretical composition $[(Cu_{0.5}Mg_{0.17})^{2+}(Fe_{0.33})^{3+}(OH)_2]\ Cl_{0.33}\ .\ xH_2O$ is thus prepared by coprecipitation at pH = 10.5. The characterization of the LDH template highlights important chemical deviation from the ideal composition underlining that a part of the cations input (Cu^{2+} and Fe^{3+}) remains in solution. The solid state material comprises LDH and a small amount of crystallized CuO, leading to the experimental LDH composition $[(Cu_{0.31}Mg_{0.38})^{2+}(Fe_{0.31})^{3+}(OH)_2]Cl_{0.31}\ .\ 0.45H_2O$. At 150°C, the formation of a LDH thermally treated by molecular F_2 phase is observed, confirming the possibility of maintaining a multi-metallic template after fluorination by topochemical reaction between hydroxides and fluorine ligands. The LDH phase is still present in small quantities after fluorination at 200°C. The transformation of the LDH phase into fluoride analogues is therefore complete shortly after 200°C with the presence of CuF_2, MgF_2 and FeF_3.

The study of the electrochemical mechanism highlights an improvement in the capacity retention compared to either FeF_3 or CuF_2, thus taking advantages of both domains while

minimizing their side-effect. The role of electrochemically inactive MgF_2 phase should be further scrutinized in future investigations by a solid solution (Mg,Cu)Fe.

Overall, the template approach shows the interest of having an intimate cation mixing for electrochemical activity in ASSB as recently reported for Prussian Blue Analogues 3D templates (Eveillard et al., 2022), with a superior behaviour observed with 2D LDH templates. Indeed, while the CuPBAs showed a capacity recovery of first charge of 59%, the LDH thermally treated by molecular F_2 showed a much higher value of redox reversibility of 76%.

FUNDING SOURCES

This work was supported by CNES.

AUTHORS CONTRIBUTIONS

Fabien Eveillard: synthesis and characterization of the materials and writing-original draft. **Nicolas Batisse:** supervisions; mass spectroscopy calculation; review. **Fabrice Leroux:** conceptualization; supervision; review and editing. **Diane Delbègue**; review and funding acquisition. **Katia Araujo da Silva:** supervision; conceptualization; review and editing. All authors have approved the final version of the manuscript.

CONFLICTS OF INTEREST

The authors declare no conflict of interest.

ACKNOWLEDGEMENTS

541 The authors acknowledge Synchrotron SOLEIL for provision of synchrotron radiation
542 facilities, and would like to thank S. Belin for measurements performed on samples on
543 beamline ROCK. They also thank M. Benbakkar from LMV (UCA, France) for conducting
544 ICP-AES measurements.

545

546 **Appendix A**

547 Electronic Supplementary Information available

548

549 **REFERENCES**

550 Behrens, M., Kasatkin, I., Kühl, S., Weinberg, G., 2010. Phase-pure Cu,Zn,Al hydrotalcite-
551 like materials as precursors for copper rich Cu/ZnO/Al_2O_3 catalysts. Chem. Mater., 22, 2,
552 386-397. https://doi.org/10.1021/cm9029165.

553 Briois, V., La Fontaine, C., Belin, S., Barthe, L., Moreno, T., Pinty, V., Carcy, A., Girardot,
554 R., Fonda, E., 2016. ROCK: The New Quick-EXAFS Beamline at SOLEIL. J. Phys.: Conf.
555 Ser., 712, 012149. https://doi:10.1088/1742-6596/712/1/012149

556 Carja, G., Nakamura, R., Aida, T., Niiyama, H., 2001. Textural Properties of Layered Double
557 Hydroxides: Effect of Magnesium Substitution by Copper or Iron. Microporous and
558 Mesoporous Materials, 47, 275–284. https://doi:10.1016/S1387-1811(01)00387-0.

559 Celik-Kucuk, A., Abe, T., 2021. Electrochemical Behavior of CuF_2 as Reversible Cathode in
560 an Organic Liquid Electrolyte for Room-Temperature Fluoride-Shuttle Batteries. Journal of
561 Power Sources, 496, 229828. https://doi:10.1016/j.jpowsour.2021.229828.

562 Chen, T.-H., Popov, I., Zenasni, O., Daugulis, O., Miljanić, O.Š., 2013. Superhydrophobic
563 Perfluorinated Metal–Organic Frameworks. Chem. Commun., 49, 6846.
564 https://doi:10.1039/c3cc41564c.

565 Constantino, V.R.L., Pinnavaia, T.J., 1995. Basic Properties of $Mg^{2+}_{1-x}Al^{3+}_{x}$ Layered Double
566 Hydroxides Intercalated by Carbonate, Hydroxide, Chloride, and Sulfate Anions. Inorg.
567 Chem., 34, 883–892. https://doi:10.1021/ic00108a020.

568 de Melo Costa-Serge, N., Gonçalves, R.G.L., Rojas-Mantilla, H.D., Santilli, C.V., Hammer,
569 P., Nogueira, R.F.P., 2021. Fenton-like Degradation of Sulfathiazole Using Copper-Modified
570 MgFe-CO_3 Layered Double Hydroxide. Journal of Hazardous Materials, 413, 125388.
571 https://doi:10.1016/j.jhazmat.2021.125388.

572 Doebelin, N., Kleeberg, R., 2015. Profex : A Graphical User Interface for the Rietveld
573 Refinement Program BGMN. J Appl Crystallogr., 48, 1573–1580.
574 https://doi:10.1107/S1600576715014685.

575 Eveillard, F., Gervillié, C., Taviot-Guého, C., Leroux, F., Guérin, K., Sougrati, M.T., Belin,
576 S., Delbègue, D., 2020. Unravelling Lithiation Mechanisms of Iron Trifluoride by Operando
577 X-Ray Absorption Spectroscopy and MCR-ALS Chemometric Tools. New J. Chem.,
578 10.1039.C9NJ06321H. https://doi:10.1039/C9NJ06321H.

579 Eveillard, F., Leroux, F., Batisse, N., Delbègue, D., Guérin, K., 2022. Copper-Iron Ternary
580 Metal Fluorides from Multi-Metallic Template Fluorination and Their First Use as Cathode in
581 Solid State Li-Batteries. Journal of Solid State Chemistry, 310, 123031.
582 https://doi:10.1016/j.jssc.2022.123031.

583 Fan, X., Luo, C., Lamb, J., Zhu, Y., Xu, K., Wang, C., 2015. PEDOT Encapsulated FeOF
584 Nanorod Cathodes for High Energy Lithium-Ion Batteries. Nano Lett., 15, 7650–7656.
585 https://doi:10.1021/acs.nanolett.5b03601.

586 Fleet, M.E., 1975. The Crystal Structure of Paratacamite, $Cu_2(OH)_3Cl$. Acta Crystallogr B
587 Struct. Sci., 31, 183–187. https://doi:10.1107/S0567740875002324.

588 Fujita, W., Awaga, K., 1997. Reversible Structural Transformation and Drastic Magnetic
589 Change in a Copper Hydroxides Intercalation Compound. J. Am. Chem. Soc., 119, 4563–
590 4564. https://doi:10.1021/ja970239o.

591 Głowniak, S., Szczęśniak, B., Choma, J., Jaroniec, M., 2021. Mechanochemistry: Toward
592 Green Synthesis of Metal–Organic Frameworks. Materials Today, 46, 109–124.
593 https://doi:10.1016/j.mattod.2021.01.008.

594 Guérin, K., Delbègue, D., Louvain, N., Doubtsof, L., Hamwi, A., Laik, B., Pereira-Ramos, J.-
595 P., Tahar-sougrati, M., Jumas, J.-C., Willmann, P., et al., 2016. Rhombohedral Iron
596 Trifluoride with a Hierarchized Macroporous/Mesoporous Texture from Gaseous Fluorination
597 of Iron Disilicide. Materials Chemistry and Physics, 173, 355–363.
598 https://doi:10.1016/j.matchemphys.2016.02.023.

599 Guo, Y., Zhu, Z., Qiu, Y., Zhao, J. 2012. Adsorption of Arsenate on Cu/Mg/Fe/La Layered
600 Double Hydroxide from Aqueous Solutions. Journal of Hazardous Materials, 239–240, 279–
601 288. https://doi:10.1016/j.jhazmat.2012.08.075.

602 Hansen, H.C.B., Koch, C.B., 1995. Synthesis and characterization of pyroaurite. Applied Clay
603 Sci., 10, 5-19. https://doi.org/10.1016/0169-1317(95)00014-U.

604 Haendler, H.M., Towle, L.H., Bennett, E.F., Patterson, W.L., 1954. The Reaction of Fluorine
605 with Copper and Some of Its Compounds. Some Properties of Copper(II) Fluoride 1. J. Am.
606 Chem. Soc., 76, 2178–2179. https://doi:10.1021/ja01637a039.

607 Hua, X., Robert, R., Du, L.-S., Wiaderek, K.M., Leskes, M., Chapman, K.W., Chupas, P.J.,
608 Grey, C.P., 2014. Comprehensive Study of the CuF_2 Conversion Reaction Mechanism in a
609 Lithium Ion Battery. J. Phys. Chem. C, 118, 15169–15184. https://doi:10.1021/jp503902z.

610 Hua, X., Eggeman, A.S., Castillo-Martínez, E., Robert, R., Geddes, H.S., Lu, Z., Pickard,
611 C.J., Meng, W., Wiaderek, K.M., Pereira, N., Amatucci, G.G., Midgley, P.A., Chaman, K.W.,
612 Steiner, U., Goodwin, A.L., Grey, C.P., 2021. Revisiting Metal Fluorides as Lithium-Ion
613 Battery Cathodes. Nat. Mater., 20, 841-850. https://doi:10.1038/s41563-020-00893-1.

614 Huang, J., Yang, Z., Wang, R., Zhang, Z., Feng, Z., Xie, X., 2015. Zn–Al Layered Double
615 Oxides as High-Performance Anode Materials for Zinc-Based Secondary Battery. J. Mater.
616 Chem. A, 3, 7429–7436. https://doi:10.1039/C5TA00279F.

617 Huang, Q., Turcheniuk, K., Ren, X., Magasinski, A., Song, A.-Y., Xiao, Y., Kim, D., Yushin,
618 G., 2019. Cycle Stability of Conversion-Type Iron Fluoride Lithium Battery Cathode at
619 Elevated Temperatures in Polymer Electrolyte Composites. Nat. Mater., 18, 1343–1349.
620 https://doi:10.1038/s41563-019-0472-7.

621 Intissar, M., Seron, A., Giovannelli, F., Autret, C., Motelica-Heino, M., Delorme, F., 2015.
622 Effect of copper content on the synthesis and properties of $(Mg_{4-x}Cu_x)Al_2OH_{12}CO_3$, nH_2O
623 layered double hydroxides. Journal of Materials Science, 50 (3), 1427-1434.
624 https://DOI:10.1007/s10853-014-8702-5.

625 Jang, W., Yoo, S., Song, J., Kim, J., An, K., Cho, S., 2021. Selective phase transformation of
626 layered double hydroxides into mixed metal oxides for catalytic CO oxidation. Cell Reports
627 Physical Science, 2, 100628. https://doi.org/10.1016/j.xcrp.2021.100628.

628 Jiménez-López, A., Rodríguez-Castellón, E., Olivera-Pastor, P., Maireles-Torres, P.,
629 Tomlinson, A.A.G., Jones, D.J., Rozière, J., 1993. Layered Basic Copper Anion Exchangers:

630 Chemical Characterisation and X-Ray Absorption Study. J. Mater. Chem., 3, 303–307.
631 https://doi:10.1039/JM9930300303.

632 Johnson, G.K., 1981. The enthalpy of formation of FeF3 by fluorine bomb calorimetry. The
633 Journal of Chemical Thermodynamics, 13 (5), 465-469. https://doi.org/10.1016/0021-
634 9614(81)90054-9.

635 Kemnitz, E., Noack, J., 2015. The non-aqueous fluorolytic sol-gel synthesis of nanoscaled
636 metal fluorides. Dalton Trans., 44, 19411-19431. https://doi.org/10.1039/C5DT00914F.

637 Krahl, T., Marroquin Winkelmann, F., Martin, A., Pinna, N., Kemnitz, E., 2018. Novel
638 Synthesis of Anhydrous and Hydroxylated CuF_2 Nanoparticles and Their Potential for
639 Lithium Ion Batteries. Chem. Eur. J., 24, 7177–7187. https://doi:10.1002/chem.201800207.

640 Lee, H.J., Park, Y.J., 2013. Interface Characterization of MgF_2-Coated $LiCoO_2$ Thin Films.
641 Solid State Ionics, 230, 86–91. https://doi:10.1016/j.ssi.2012.08.003.

642 Lemoine, K., Moury, R., Durand, E., Dompablo, E.A., Morán, E., Leblanc, M., Hémon-
643 Ribaud, A., Grenèche, J.-M., Galven, C., Gunes, V., et al., 2021. First Mixed-Metal Fluoride
644 Pyrochlores Obtained by Topotactic Oxidation of Ammonium Fluorides under F_2 Gas. Crystal
645 Growth & Design, 21, 935–945. https://doi:10.1021/acs.cgd.0c01279.

646 Leroux, F., Roussel, H., Flank, A.-M., Briois, V., 2002. Local Order of the Transition Metals
647 for the Substitution $(Co_{1-y}Cu_y)_2Al(OH)_6Cl\cdot nH_2O$ ($0 \leq y \leq 1$) in a Copper-Aluminum-Layered
648 Double Hydroxide-like Phase. Clays and Clay Minerals, 50, 254–264.
649 https://doi:10.1346/000986002760832856.

650 Liu, H., Zha, M., Liu, Z., Tian, J., Hu, G., Feng, L., 2020. Synergistically Boosting the
651 Oxygen Evolution Reaction of an Fe-MOF via Ni Doping and Fluorination. Chem. Commun.,
652 56, 7889–7892. https://doi:10.1039/D0CC03422C.

Louvain, N., Peyroux, J., Dubois, M., Simond, W., Leroux, F., 2014. Efficient Fluorinating Agent through Topochemical Fluorination of Co–Fe Layered Double Hydroxides. Inorg. Chem., 53, 852–860. https://doi:10.1021/ic402193x.

Lu, H., Zhu, Z., Zhang, H., Zhu, J., Qiu, Y., Zhu, L., Küppers, S., 2016. Fenton-Like Catalysis and Oxidation/Adsorption Performances of Acetaminophen and Arsenic Pollutants in Water on a Multimetal Cu–Zn–Fe-LDH. ACS Appl. Mater. Interfaces, 8, 25343–25352. https://doi:10.1021/acsami.6b08933.

Lu, H., Sui, M., Yuan, B., Wang, J., Lv, Y., 2019. Efficient Degradation of Nitrobenzene by Cu-Co-Fe-LDH Catalyzed Peroxymonosulfate to Produce Hydroxyl Radicals. Chemical Engineering Journal, 357, 140–149. https://doi:10.1016/j.cej.2018.09.111.

Myung, S.-T., Sakurada, S., Yashiro, H., Sun, Y.-K., 2013. Iron Trifluoride Synthesized via Evaporation Method and Its Application to Rechargeable Lithium Batteries. Journal of Power Sources, 223, 1–8. https://doi:10.1016/j.jpowsour.2012.09.027.

Nejati, K., Davary, S., Saati, M. 2013. Study of 2,4-Dichlorophenoxyacetic Acid (2,4-D) Removal by Cu-Fe-Layered Double Hydroxide from Aqueous Solution. Applied Surface Science, 280, 67–73. https://doi:10.1016/j.apsusc.2013.04.086.

Omenya, F., Zagarella, N.J., Rana, J., Zhang, H., Siu, C., Zhou, H., Wen, B., Chernova, N.A., Piper, L.F.J., Zhou, G., Whittingham, M.S., 2019. Intrinsic Challenges to the Electrochemical Reversibility of the High Energy Density Copper(II) Fluoride Cathode Material. ACS Appl. Energy Mater., 2, 5243–5253. https://doi:10.1021/acsaem.9b00938.

Pachfule, P., Chen, Y., Sahoo, S.C., Jiang, J., Banerjee, R., 2011. Structural Isomerism and Effect of Fluorination on Gas Adsorption in Copper-Tetrazolate Based Metal Organic Frameworks. Chem. Mater., 23, 2908–2916. https://doi:10.1021/cm2004352.

Pachfule, P., Garai, B., Banerjee, R., 2016. Functionalization and Isoreticulation in a Series of Metal–Organic Frameworks Derived from Pyridinecarboxylates. Inorg. Chem., 55, 7200–7205. https://doi:10.1021/acs.inorgchem.6b00758.

Ravel, B., Newville, M., 2005. ATHENA , ARTEMIS , HEPHAESTUS : Data Analysis for X-Ray Absorption Spectroscopy Using IFEFFIT. J. Synchrotron Rad., 12, 537–541. https://doi:10.1107/S0909049505012719.

Rozov, K., Berner, U., Taviot-Gueho, C., Leroux, F., Renaudin, G., Kulik, D., Diamond, L.W., 2010. Synthesis and characterization of the LDH hydrotalcite-pyroaurite solide-solution series. Cement Concrete Res. 40, 1248-1254. https://doi.org/10.1016/j.cemconres.2009.08.031.

Rudzitis, E., Feder, H.M., Hubbard, W.N., 1964. Fluorine Bomb Calorimetry. IX. The Enthalpy of Formation of Magnesium Difluoride. J. Phys. Chem., 68, 10, 2978-2981. https://doi.org/10.1021/j100792a041.

Seo, J.K., Cho, H.-M., Takahara, K., Chapman, K.W., Borkiewicz, O.J., Sina, M., Shirley Meng, Y., 2017. Revisiting the Conversion Reaction Voltage and the Reversibility of the CuF_2 Electrode in Li-Ion Batteries. Nano Res., 10, 4232–4244. https://doi:10.1007/s12274-016-1365-6.

Shimoda, K., Shikano, M., Murakami, M., Sakaebe, H., 2020. Capacity Fading Mechanism of Conversion-Type FeF3 Electrode: Investigation by Electrochemical Operando Nuclear Magnetic Resonance Spectroscopy. Journal of Power Sources, 477, 228772. https://doi:10.1016/j.jpowsour.2020.228772.

Skapin, T., Tavčar, G., Benčan, A., Mazej, Z., 2009. Recent Developments in the Preparation of High Surface Area Metal Fluorides. Journal of Fluorine Chemistry, 130, 1086–1092. https://doi:10.1016/j.jfluchem.2009.06.015.

Sun, F., Li, Q., Xue, H., Pang, H., 2019. Pristine Transition- Metal- Based Metal- Organic Frameworks for Electrocatalysis. ChemElectroChem, 6, 1273–1299. https://doi:10.1002/celc.201801520.

Taviot-Guého, C., Prévot, V., Forano, C., Renaudin, G., Mousty, C., Leroux, F., 2018. Tailoring Hybrid Layered Double Hydroxides for the Development of Innovative Applications. Adv. Funct. Mater., 28, 1703868. https://doi:10.1002/adfm.201703868.

Turcheniuk, K., Bondarev, D., Amatucci, G.G., Yushin, G., 2021. Battery Materials for Low-Cost Electric Transportation. Materials Today, 42, 57–72. https://doi:10.1016/j.mattod.2020.09.027.

Walsh, A., Catlow, C.R.A., Galvelis, R., Scanlon, D.O., Schiffmann, F., Sokol, A.A., Woodley, S.M., 2012. Prediction on the existence and chemical stability of cuprous fluoride. Chemical Science, 3, (8), 2565-2569. https://doi.org/10.1039/c2sc20321a.

Wang, F., Kim, S.-W., Seo, D.-H., Kang, K., Wang, L., Su, D., Vajo, J.J., Wang, J., Graetz, J., 2015. Ternary Metal Fluorides as High-Energy Cathodes with Low Cycling Hysteresis. Nature Communications, 6, 6668. https://doi:10.1038/ncomms7668.

Wang, H., Jing, M., Wu, Y., Chen, W., Ran, Y., 2018. Effective Degradation of Phenol via Fenton Reaction over CuNiFe Layered Double Hydroxides. Journal of Hazardous Materials, 353, 53–61. https://doi:10.1016/j.jhazmat.2018.03.053.

Wang, S., Hu, T., Wang, G., Wang, Z., Yan, D., Liang, R., Tan, C., 2021. Ultrathin $CuFe_2S_3$ Nanosheets Derived from CuFe-Layered Double Hydroxide as an Efficient Nanoagent for Synergistic Chemodynamic and NIR-II Photothermal Therapy. Chemical Engineering Journal, 419, 129458. https://doi:10.1016/j.cej.2021.129458.

722 Wu, Q., Zhang, X., Sun, S., Wan, N., Pan, D., Bai, Y., Zhu, H., Hu, Y.-S., Dai, S., 2015.
723 Improved Electrochemical Performance of Spinel $LiMn_{1.5}Ni_{0.5}O_4$ through MgF_2 Nano-
724 Coating. Nanoscale, 7, 15609–15617. https://doi:10.1039/C5NR03564C.

725 Wu, F., Maier, J., Yu, Y., 2020a. Guidelines and Trends for Next-Generation Rechargeable
726 Lithium and Lithium-Ion Batteries. Chem. Soc. Rev., 49, 1569–1614.
727 https://doi:10.1039/C7CS00863E.

728 Wu, L., Peng, B., Li, Q, Wang, Q., Yan, X., Li, K., Lin, Q., 2020b. Effects of Cu^{2+}
729 incorporation on ZnAl-layered double hydroxide. New J. Chem., 44, 5293-5302.
730 https://doi.org/10.1039/D0NJ00278J.

731 Wu, F., Srot, V., Chen, S., Zhang, M., van Aken, P.A., Wang, Y., Maier, J., Yu, Y., 2021.
732 Metal–Organic Framework-Derived Nanoconfinements of CoF_2 and Mixed-Conducting
733 Wiring for High-Performance Metal Fluoride-Lithium Battery. ACS Nano, 15, 1509–1518.
734 https://doi:10.1021/acsnano.0c08918.

735 Xia, Z., An, L., Chen, P., Xia, D., 2016. Non-Pt Nanostructured Catalysts for Oxygen
736 Reduction Reaction: Synthesis, Catalytic Activity and Its Key Factors. Adv. Energy Mater., 6,
737 1600458. https://doi:10.1002/aenm.201600458.

738 Xu, Q., Yang, X., Rao, M., Lin, D., Yan, K., Du, R., Xu, J., Zhang, Y., Ye, D., Yang, S., et
739 al., 2020. High Energy Density Lithium Metal Batteries Enabled by a Porous Graphene/MgF_2
740 Framework. Energy Storage Materials, 26, 73–82. https://doi:10.1016/j.ensm.2019.12.028.

741 Zang, P., Liu, J., He, Y., Zhang, G., Li, G., Wang, Y., Lv, Y., 2022. LDH-Derived
742 Preparation of CuMgFe Layered Double Oxides for NH_3-SCR and CO Oxidation Reactions:
743 Performance Study and Synergistic Mechanism. Chemical Engineering Journal, 446, 137414.
744 https://doi:10.1016/j.cej.2022.137414.

745 Zhang, Q., Liu, N., Sun, C., Fan, L., Zhang, N., Sun, K., 2019. Ultrasmall Iron Fluoride
746 Nanoparticles Embedded in Graphitized Porous Carbon Derived from Fe- Based Metal
747 Organic Frameworks as High- Performance Cathode Materials for Li Batteries.
748 ChemElectroChem, 6, 2189–2194. https://doi:10.1002/celc.201900244.

749 Zhu, J., Deng, D., 2015. Wet-Chemical Synthesis of Phase-Pure FeOF Nanorods as High-
750 Capacity Cathodes for Sodium-Ion Batteries. Angew. Chem. Int. Ed., 54, 3079–3083.
751 https://doi:10.1002/anie.201410572.

752 Zubair, M., Aziz, H.A., Ihsanullah, I., Ahmad, M.A., Al-Harthi, M.A., 2021. Biochar
753 Supported CuFe Layered Double Hydroxide Composite as a Sustainable Adsorbent for
754 Efficient Removal of Anionic Azo Dye from Water. Environmental Technology &
755 Innovation, 23, 101614. https://doi:10.1016/j.eti.2021.101614.